

A Comparison of Multi-Frame Blind Deconvolution and Speckle Imaging Energy Spectrum Signal-to-Noise Ratios-- Journal Article (Preprint)

Charles L. Matson

11 September 2008

Technical Paper

APPROVED FOR PUBLIC RELEASE; DISTRIBUTION IS UNLIMITED.



**AIR FORCE RESEARCH LABORATORY
Directed Energy Directorate
3550 Aberdeen Ave SE
AIR FORCE MATERIEL COMMAND
KIRTLAND AIR FORCE BASE, NM 87117-5776**

REPORT DOCUMENTATION PAGE				Form Approved OMB No. 0704-0188	
Public reporting burden for this collection of information is estimated to average 1 hour per response, including the time for reviewing instructions, searching existing data sources, gathering and maintaining the data needed, and completing and reviewing this collection of information. Send comments regarding this burden estimate or any other aspect of this collection of information, including suggestions for reducing this burden to Department of Defense, Washington Headquarters Services, Directorate for Information Operations and Reports (0704-0188), 1215 Jefferson Davis Highway, Suite 1204, Arlington, VA 22202-4302. Respondents should be aware that notwithstanding any other provision of law, no person shall be subject to any penalty for failing to comply with a collection of information if it does not display a currently valid OMB control number. PLEASE DO NOT RETURN YOUR FORM TO THE ABOVE ADDRESS.					
1. REPORT DATE (DD-MM-YYYY) 11-09-2008		2. REPORT TYPE Technical Paper		3. DATES COVERED (From - To) Jan 1, 2007- Sept 11, 2008	
4. TITLE AND SUBTITLE A Comparison of Multi-Frame Blind Deconvolution and Speckle Imaging Energy Spectrum Signal-to-Noise Ratios--Journal Article (Preprint)				5a. CONTRACT NUMBER In House -701944	
				5b. GRANT NUMBER	
				5c. PROGRAM ELEMENT NUMBER 61102F	
6. AUTHOR(S) Charles L. Matson				5d. PROJECT NUMBER 2311	
				5e. TASK NUMBER S3	
				5f. WORK UNIT NUMBER 01	
7. PERFORMING ORGANIZATION NAME(S) AND ADDRESS(ES) AFRL/RDSA 3550 Aberdeen Ave. SE Kirtland AFB, NM 87117-5776				8. PERFORMING ORGANIZATION REPORT NUMBER	
9. SPONSORING / MONITORING AGENCY NAME(S) AND ADDRESS(ES) Air Force Research Laboratory 3550 Aberdeen Ave SE Kirtland AFB NM 87117-5776				10. SPONSOR/MONITOR'S ACRONYM(S) AFRL/RDSA	
				11. SPONSOR/MONITOR'S REPORT NUMBER(S) AFRL-RD-PS-TP-2008-1005	
12. DISTRIBUTION / AVAILABILITY STATEMENT Approved for public release; Distribution is Unlimited.					
13. SUPPLEMENTARY NOTES Accepted for publication in the SPIE proceedings Vol. 7108, Fall 2008. "Government Purpose Rights"					
14. ABSTRACT An analytical signal-to-noise ratio (SNR) expression is derived for unbiased estimates of energy spectra obtained using multi-frame blind deconvolution (MFBD) algorithms. Because an analytical variance expression cannot, in general, be derived, Cramer-Rao lower bounds are used in place of the variances. As a result, the SNR expression provided upper bounds to the achievable SNR's that are independent of the NFBD algorithm implementation. The SNR expression is evaluated for the scenario of ground-based imaging of astronomical objects. It is shown that MFBD energy-spectrum SNR's are usually greater, and often much greater, than their corresponding speckle imaging (SI) energy spectrum SNRs at all spatial frequencies. One reason for the SNR disparity is that SI energy spectrum SNRs are proportional to the object energy spectrum and the ensemble-averaged atmosphere energy spectrum, while MFBD SNRs are approximately proportional to the square root of these quantities.					
15. SUBJECT TERMS blind deconvolution, speckle imaging, signal-to-noise ratios, Cramer-Rao lower bounds					
16. SECURITY CLASSIFICATION OF:			17. LIMITATION OF ABSTRACT SAR	18. NUMBER OF PAGES 14	19a. NAME OF RESPONSIBLE PERSON Charles L. Matson
a. REPORT Unclassified	b. ABSTRACT Unclassified	c. THIS PAGE Unclassified			19b. TELEPHONE NUMBER (include area code) 505- 846-2049

Standard Form 298 (Rev. 8-98)
Prescribed by ANSI Std. Z39.18

A comparison of multi-frame blind deconvolution and speckle imaging energy spectrum signal-to-noise ratios

Charles L. Matson

Directed Energy Directorate, Air Force Research Laboratory, Kirtland AFB, NM USA 87117

ABSTRACT

An analytical signal-to-noise ratio (SNR) expression is derived for unbiased estimates of energy spectra obtained using multi-frame blind deconvolution (MFBD) algorithms. Because an analytical variance expression cannot, in general, be derived, Cramér-Rao lower bounds are used in place of the variances. As a result, the SNR expression provides upper bounds to the achievable SNRs that are independent of the MFBD algorithm implementation. The SNR expression is evaluated for the scenario of ground-based imaging of astronomical objects. It is shown that MFBD energy-spectrum SNRs are usually greater, and often much greater, than their corresponding speckle imaging (SI) energy-spectrum SNRs at all spatial frequencies. One reason for this SNR disparity is that SI energy spectrum SNRs are proportional to the object energy spectrum and the ensemble-averaged atmosphere energy spectrum, while MFBD SNRs are approximately proportional to the square root of these quantities. Another reason for this SNR disparity is that single-frame SI energy-spectrum SNRs are limited above by one, while the MFBD energy-spectrum SNRs are not.

Keywords: blind deconvolution, speckle imaging, signal-to-noise ratios, Cramér-Rao lower bounds

1. INTRODUCTION

The spatial resolutions of visible-wavelength astronomical images obtained using meter-class or larger ground-based telescopes are greatly affected by atmospheric turbulence.¹ Because of this fact, post-processing algorithms are often used to remove atmospheric blurring from a sequence of short-exposure images of an astronomical object. The object is assumed to remain the same for all the short-exposure images, but the atmospheric point-spread functions (PSFs) are different for each short exposure image. The term “short exposure” means that integration times for the images are comparable to or shorter than the coherence time of the atmosphere. Multi-frame blind deconvolution (MFBD)^{2,3} and speckle imaging (SI)¹ algorithms are arguably the most common types of algorithms used for this purpose. MFBD and SI algorithms take distinctly different approaches to removing atmospheric turbulence, however. SI algorithms estimate image quantities that, when averaged over the sequence of short-exposure images, retain high spatial frequency information about the object. The most commonly estimated quantities are the images’ average energy spectrum, cross-spectrum, and bispectrum. A sequence of short exposure images of an unresolved star is needed in addition to the sequence of short exposure images of the object in order to estimate and remove the atmospheric contributions to these quantities. MFBD algorithms, on the other hand, treat the individual PSFs of the short exposure images of the object as deterministic (but unknown) functions to be estimated jointly with the underlying object, and do not require separate star measurements. Thus, MFBD algorithms estimate first-order quantities (PSF quantities and object intensities) while SI algorithms estimate second-order (energy spectrum and cross spectrum) and third-order (bispectrum) quantities. In addition, SI algorithms include more data (the unresolved star images) than do MFBD algorithms.

Because MFBD and SI algorithms are both used to deblur images, it is of interest to compare how well they accomplish this task. Such comparisons have been carried out many times in the past by visually assessing image reconstructions produced by these algorithms and qualitatively rating their quality. This approach can be misleading, however, since it is possible to have one algorithm produce a deblurred image that is of lesser visual quality than a deblurred image produced from the same data by another algorithm even if the signal-to-noise (SNR) properties of the second deblurred image are comparable to the first. For example, regularization filters significantly impact the visual quality of an image and yet do not modify the Fourier-domain SNR properties at all. Therefore, it is of value to carry out a comparison of the quality of deblurred images produced by these two algorithms using a quantitative approach. To date (to the author’s knowledge), this type of analysis has not been carried out. The probable reason for this lack of analysis is that there do not exist closed-form expressions for MFBD-based estimators, and thus no analytical expressions for the variances of these estimates, as do exist for SI.

In this paper, the quality of deblurred images produced by SI and MFBD algorithms is compared using the SNRs of unbiased estimates of energy spectra as a metric. There are at least two reasons to use this metric. First, it is possible to obtain unbiased estimates of energy spectra inside the bandpass of the optical system. Because telescopes are spatial low-pass filters, it is difficult to obtain unbiased estimates of image-domain quantities. Unbiased estimates simplify and generalize the comparison results because the effect of biases on mean-square error do not need to be taken into account. Second, the energy-spectrum SNR properties of a deblurred image can be mapped directly to the resolution in the deblurred image.

To carry out this comparison, analytical expressions for the SNRs of SI and MFBD energy spectra estimates are necessary. A closed-form expression for SI energy spectrum SNRs (hereafter referred to as SI SNRs), used in this paper, has been available for several decades and has been used extensively to predict the performance of SI-based imaging systems and to compare measurement-data results to theory.¹ For MFBD-based imaging systems, however, such an expression is not available because an analytical variance expression cannot, in general, be derived. For this reason, lower bounds to the variances of unbiased estimates of energy spectra are used for the results in this paper in place of an analytical variance expression. More specifically, Cramér-Rao lower bounds (CRBs)⁴ are used in this paper because they can often be achieved or approached closely. The use of CRBs provides an analytical, but not closed-form, SNR expression for MFBD energy spectrum estimation. For the CRB calculations, it is assumed that object support constraints are included in the estimation process. When the MFBD estimator is modeled as estimating the PSFs pixel by pixel in the image domain, PSF support constraints are also included in the CRB calculations.

A number of important properties of MFBD energy spectrum SNRs (referred to hereafter as MFBD SNRs) were uncovered as a result of this comparison study. One property is that MFBD SNRs are usually larger, and often much larger, than the associated SI SNRs. This property is a result of the fact that the SI SNRs are proportional to the object energy spectrum and the ensemble-averaged atmosphere energy spectrum (the speckle transfer function), while MFBD SNRs are approximately proportional to the square root of these quantities. A second property is that all SI SNRs are bounded above by the square root of the number of measurement frames used in the estimation process (for all spatial frequencies greater than approximately those present in long-exposure images) regardless of the number of detected photons, while MFBD SNRs are not bounded above. A third property is that MFBD SNRs are decreasing functions of the PSF and object support constraint areas, and the rates of decrease get smaller as the support constraint areas get larger.

The paper is divided into sections as follows: the imaging model is contained in Section 2, the SI and MFBD SNR expressions are given in Section 3, representative SNR plots and properties are presented and discussed in Section 4, while Section 5 contains conclusions.

2. IMAGING MODEL

The linear space-invariant imaging equation used for the results in this paper is given by

$$i_m(\mathbf{x}) = o(\mathbf{x}) * h_m(\mathbf{x}) + n_m(\mathbf{x}); m=1, \dots, M, \quad (1)$$

where $i_m(\mathbf{x})$ is the m^{th} short-exposure image, $o(\mathbf{x})$ is the true object, $h_m(\mathbf{x})$ is the m^{th} PSF, $n_m(\mathbf{x})$ is the m^{th} noise realization, M is the number of images used to reconstruct a single object estimate, \mathbf{x} is a two-dimensional spatial location vector, bold-face type indicates vector and matrix quantities, and $*$ denotes convolution. The noise term incorporates both Gaussian and Poisson noises.

In preparation for the CRB theory presented in Section 3, it is necessary to rewrite the imaging model of Eq.(1) in a discrete vector form. To this end, let $\boldsymbol{\alpha}$ be a column vector that contains the spatial locations of the intensity values of $i_m(\mathbf{x})$. Then let \mathbf{y}_m , $\boldsymbol{\theta}$, and $\boldsymbol{\eta}_m$ be column vectors that contain the values of $i_m(\boldsymbol{\alpha})$, $o(\boldsymbol{\alpha})$, and $n_m(\boldsymbol{\alpha})$, respectively, on the grid defined by $\boldsymbol{\alpha}$. In addition, let \mathbf{H}_m be the block-circulant system matrix associated with $h_m(\boldsymbol{\alpha})$.⁵ This permits rewriting Eq.(1) as a matrix-vector equation given by

$$\mathbf{y}_m = \mathbf{H}_m \boldsymbol{\theta} + \boldsymbol{\eta}_m; m=1, \dots, M. \quad (2)$$

Now let all M measurements be concatenated into a single measurement vector \mathbf{y} , where $\mathbf{y} = [\mathbf{y}_1^T, \dots, \mathbf{y}_M^T]^T$. Then the concatenated measurement equation can be written as

$$\mathbf{y} = \mathbf{H}\boldsymbol{\theta} + \boldsymbol{\eta}, \quad (3)$$

where $\mathbf{H}\boldsymbol{\theta} = [(\mathbf{H}_1\boldsymbol{\theta})^T, \dots, (\mathbf{H}_M\boldsymbol{\theta})^T]^T$, $\boldsymbol{\eta} = [\boldsymbol{\eta}_1^T, \dots, \boldsymbol{\eta}_M^T]^T$, and the PDF of $\boldsymbol{\eta}$ is denoted by $f_{\boldsymbol{\eta}}(\boldsymbol{\eta})$. Because both photon and camera read noises are statistically independent across pixels and across measurement frames, $f_{\boldsymbol{\eta}}(\boldsymbol{\eta})$ is equal to the multiplication of all the single-pixel PDFs.

3. SI AND MFBD SNR EXPRESSIONS

3.1 SI SNR expression

The image SI SNR expression at a spatial frequency \mathbf{f} , $\text{SNR}_{\text{SI}}(\mathbf{f})$, is given by¹

$$\text{SNR}_{\text{SI}} \propto M^{1/2} \frac{K^2 |O_n(\mathbf{f})|^2 E[|H(\mathbf{f})|^2]}{\left[K^2 + K^2 |O_n(\mathbf{f})|^2 E[|H(\mathbf{f})|^2] + 2K^3 |O_n(\mathbf{f})|^2 E[|H(\mathbf{f})|^2] + K^4 |O_n(\mathbf{f})|^2 E[|H(\mathbf{f})|^2]^2 + N^4 \sigma^4 \right]^{1/2}} \quad (4)$$

where K is the mean number of photons per short-exposure image, $|O_n(\mathbf{f})|$ is the Fourier amplitude spectrum of $o(\mathbf{x})$ normalized to one at zero spatial frequency, $E[|H(\mathbf{f})|^2]$ is the speckle transfer function that is one at zero spatial frequency,¹ N^2 is the number of pixels in each short-exposure image, and σ^2 is the single-pixel variance of the camera Gaussian read noise. This expression for $\text{SNR}_{\text{SI}}(\mathbf{f})$ is valid for spatial frequencies greater than r_0/λ , where r_0 is the coherence length of the atmosphere and λ is the imaging wavelength.

Equation (4) is the SNR expression for the estimated image energy spectrum, not for the estimated object energy spectrum. If a high-SNR and unbiased estimate of $E[|H(\mathbf{f})|^2]$ is available, $\text{SNR}_{\text{SI}}(\mathbf{f})$ is also the SNR expression for the estimated object energy spectrum if the object energy spectrum is estimated by dividing the image energy spectrum estimate by $E[|H(\mathbf{f})|^2]$. In practice, this is typically how an estimate of $|O(\mathbf{f})|^2$ is obtained, where $E[|H(\mathbf{f})|^2]$ is calculated using separate measurements of an unresolved star. Although this assumption is a good one in practice, there is still noise associated with estimating $E[|H(\mathbf{f})|^2]$. For this reason, the SNR expression in Eq.(4) provides upper bounds to the achievable SNRs for $E[|O(\mathbf{f})|^2]$.

3.2 MFBD SNR expression

The MFBD SNR expression at a spatial frequency \mathbf{f} , $\text{SNR}_{\text{MFBD}}(\mathbf{f})$, is given by

$$\text{SNR}_{\text{MFBD}} \propto \frac{K^2 |O_n(\mathbf{f})|^2}{[\text{CRB}_{\text{ES}}(\mathbf{f})]^2} \quad (5)$$

where $\text{CRB}_{\text{ES}}(\mathbf{f})$ is the MFBD-based object energy spectrum CRB at the spatial frequency \mathbf{f} . The numerator in Eq.(5) is the result of assuming an unbiased estimate of $|O_n(\mathbf{f})|^2$. There is no closed-form expression for $\text{CRB}_{\text{ES}}(\mathbf{f})$; however, the process used to calculate $\text{CRB}_{\text{ES}}(\mathbf{f})$ is outlined below.

Consider first the general problem of calculating the CRBs associated with estimating a vector of parameters $\boldsymbol{\Phi}$ based on a measurement vector \mathbf{y} that has a probability density function $f(\mathbf{y}; \boldsymbol{\Phi})$ that is a function of the unknown parameter vector $\boldsymbol{\Phi}$. These CRBs are the diagonal elements of the inverse of the Fisher Information Matrix (FIM), \mathbf{F} , whose value in the p^{th} row and q^{th} column, F_{pq} , is given by

$$\mathbf{F}_{pq} = E \left[\frac{\partial \ln f(\mathbf{y}; \boldsymbol{\Phi})}{\partial \Phi_p} \frac{\partial \ln f(\mathbf{y}; \boldsymbol{\Phi})}{\partial \Phi_q} \right], \quad (6)$$

where $\ln()$ is the natural logarithm of the quantity in parentheses, and Φ_p is the p^{th} element of $\boldsymbol{\Phi}$. Often it is of interest to generate CRBs for a function $\mathbf{g}(\boldsymbol{\Phi})$ of the parameters in terms of the FIM associated with $\boldsymbol{\Phi}$ because it makes the calculations easier. In this case, the CRBs associated with $\mathbf{g}(\boldsymbol{\Phi})$ are the diagonal elements of the matrix $\mathbf{G}\mathbf{F}^{-1}\mathbf{G}^T$, where \mathbf{G} is the Jacobian of \mathbf{g} .

Based on the theory in the preceding paragraph, the object energy spectrum CRBs are calculated in four steps. The first step is calculating the FIM associated with jointly estimating all object image-domain intensity values and all M sets of PSF parameter values inside their respective support constraint regions. The second step is inverting this FIM. The third step is calculating the matrix $\mathbf{G}\mathbf{F}^{-1}\mathbf{G}^T$, where \mathbf{G} is the Jacobian associated with the function \mathbf{g} that transforms the object intensity values into object energy spectrum values. The fourth and final step is to extract the diagonal elements of $\mathbf{G}\mathbf{F}^{-1}\mathbf{G}^T$ that are the object energy spectrum CRBs. The FIM contains terms associated with estimating both of the object and PSF parameter values because MFBD algorithms jointly estimate both object and PSF parameters. The object parameters are its image-domain intensities, while there are two types of PSF parameterizations that are used for the results in this paper. The first is in terms of the image-domain PSF intensity values (pixel-based PSF parameterization), while the second is in terms of the coefficients of a Zernike expansion of the pupil E-field phase that are associated with the PSF (Zernike-based PSF parameterization). The vector Φ in Eq.(6) contains all of the object parameters and all M sets of PSF parameters.

The general form of \mathbf{F} for MFBD-based estimation is given by

$$\mathbf{F} = \begin{bmatrix} \mathbf{F}_{11} & \cdot & \cdot & \cdot & \mathbf{F}_{1\langle M+1 \rangle} \\ \cdot & \cdot & \cdot & \mathbf{0} & \cdot \\ \cdot & \cdot & \cdot & \cdot & \cdot \\ \cdot & \mathbf{0} & \cdot & \cdot & \cdot \\ \mathbf{F}_{\langle M+1 \rangle 1} & \cdot & \cdot & \cdot & \mathbf{F}_{\langle M+1 \rangle \langle M+1 \rangle} \end{bmatrix}. \quad (7)$$

\mathbf{F}_{11} is the block of \mathbf{F} associated with the object parameters, \mathbf{F}_{p1} and \mathbf{F}_{1p} for $p>1$ are the blocks of \mathbf{F} that contain the cross-terms of object parameters and the $(p-1)^{\text{th}}$ PSF parameters, and \mathbf{F}_{pp} for $p>1$ is the block of \mathbf{F} associated with the $(p-1)^{\text{th}}$ PSF parameters.

4. RESULTS

Results from evaluating and comparing the SI SNRs and MFBD SNRs using Eqs.(4) and (5) are presented in this section. Subsections 4.1 – 4.5 contain descriptions of the SI SNR and MFBD SNR dependencies on $|\mathbf{O}_n(\mathbf{f})|^2 \mathbf{E}[\mathbf{H}(\mathbf{f})]^2$, D/r_o (where D is the telescope diameter), K , object support constraint area, and PSF support constraint area, respectively. The SNR calculations were carried out for the two objects shown in Fig. 1; for $D/r_o = 8, 16$, and 32 ; for $K = 10^2, 10^4$, and 10^8 ; and for various object support constraint areas. The atmospheric PSFs for the results in this section were created with the use of Kolmogorov-based random phase screens generated using a 100-term Zernike expansion of the pupil phase. For the MFBD SNR calculations, the PSFs were parameterized in two different ways: a 100-term Zernike expansion of the pupil phase, and in terms of the image-domain intensity values. For Zernike-based PSF parameterization, no PSF support constraint was used. For pixel-based PSF parameterization, various PSF circular support constraints were used. All the results in Subsections 4.1 – 4.5 assume that the photon noise dominates the read noise (i.e., the SNRs are independent of the value of the read noise) and that $M=10$. The impacts of read noise dominating photon noise and of the value of M on the SNRs are discussed in Subsection 4.6.

4.1 SNR dependence on $|\mathbf{O}_n(\mathbf{f})|^2 \mathbf{E}[\mathbf{H}(\mathbf{f})]^2$

In this subsection it is shown that the functional dependence of the MFBD SNRs on spatial frequency is approximately proportional to the square root of $|\mathbf{O}_n(\mathbf{f})|^2 \mathbf{E}[\mathbf{H}(\mathbf{f})]^2$ for all but the highest and lowest spatial frequency magnitudes. For ease of understanding, the SNRs are plotted as a function of spatial frequency magnitude normalized to one at D/λ . All plots are for the OCNR object, an object support constraint region that was generated by blurring the true object support with a 2 by 2 kernel (blur2 support), and for $K = 10^4$. A circular PSF support constraint region that contained 99.9% of the PSF energy was used for the pixel-based PSF parameterization. For each of the MFBD SNR plots, there is a corresponding plot of the square root of $|\mathbf{O}_n(\mathbf{f})|^2 \mathbf{E}[\mathbf{H}(\mathbf{f})]^2$ that is scaled in amplitude to a best fit visually to the MFBD SNR plot.

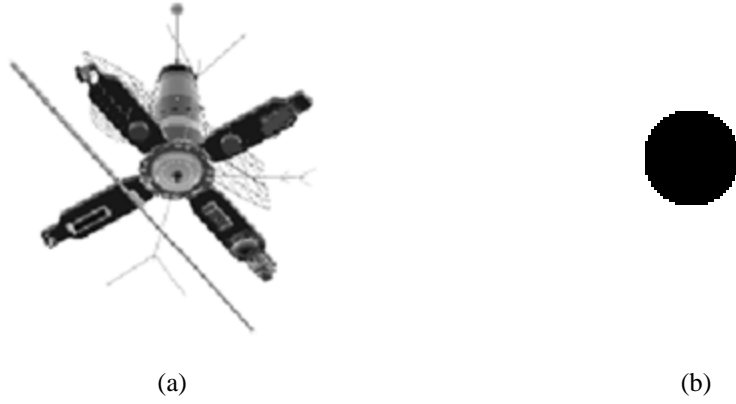


Fig. 1. Objects used for SNR calculations: (a) OCNR, (b) disc.

Figure 2 contains arbitrarily-scaled MFBF SNR plots for $D/r_o = 8$ and 32. The purpose of these plots is to illustrate the spatial-frequency dependence of the SNRs; thus, the plots are scaled to clarify this dependence. Only the relative y-axis values for each pair of plots are meaningful. For each of these D/r_o values, there are plots for both Zernike-based and pixel-based PSF parameterization. The proportionality of the SNRs to the square root of $|O_n(f)|^2 E[H(f)]^2$ is quite good except for the highest and lowest spatial frequencies for both D/r_o ratios and for both PSF parameterizations. Similar results are obtained when varying other parameters such as the object, object support constraint area, PSF support constraint area (for pixel-based PSF parameterization), and photon levels. In contrast, it can be seen from Eq.(4) that the SI SNRs are proportional to $|O_n(f)|^2 E[H(f)]^2$, not its square root, at low light levels (i.e., when the denominator is dominated by the K^2 term). In the high-light level limit, (i.e., when the denominator of Eq.(4) is dominated by the $K^4 |O_n(f)|^4 E[H(f)]^2$ term), the SI SNRs are independent of $|O_n(f)|^2 E[H(f)]^2$.

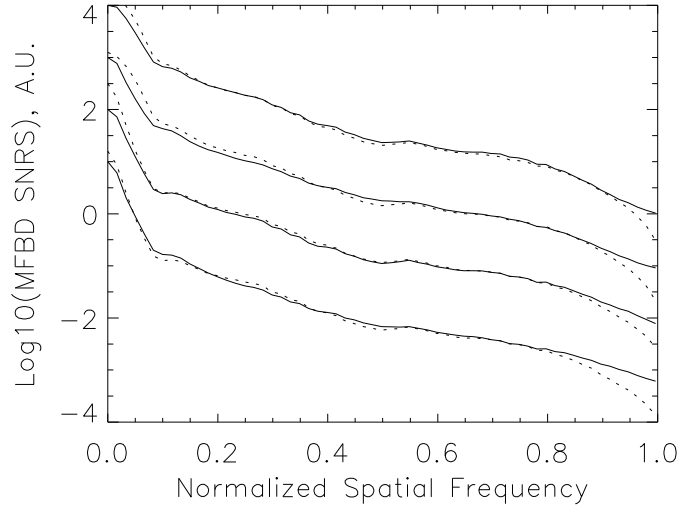


Fig. 2. Log_{10} plots of MFBF SNRs (solid lines) and the square root of $|O_n(f)|^2 E[H(f)]^2$ (dotted lines) in arbitrary units versus normalized spatial frequency magnitude. Parameter values are $K = 10^4$, OCNR object, and blur2 object support constraint for all plots. In addition, a 99.9% circular PSF support constraint was used for pixel-based PSF parameterization. From top to bottom, the parameters for each pair of lines are: $D/r_o = 8$, Zernike-parameterized PSF; $D/r_o = 8$, pixel-parameterized PSF; $D/r_o = 32$, Zernike-parameterized PSF; $D/r_o = 32$, pixel-parameterized PSF. The line pairs are shifted vertically for clarity.

Plots of absolute (not relative) SI SNRs and the MFBD SNRs for both pixel-based and Zernike-based PSF parameterization are shown in Fig. 3. The parameters for these plots are $D/r_o = 8$, $K = 10^4$, the OCNR object, blur2 object support constraint, and the 99.9% circular PSF support constraint for pixel-based PSF parameterization. Notice that the MFBD SNRs for Zernike-based PSF parameterization are the highest, followed by the MFBD SNRs for pixel-based PSF parameterization, followed by the SI SNRs. It was expected that the MFBD SNRs would be higher for Zernike-based PSF parameterization than for pixel-based PSF parameterization because there are fewer Zernike coefficients to be estimated than PSF pixel values; however, it was surprising to see that the SI SNRs fared as poorly as they did against the MFBD SNRs. Although the MFBD SNRs are higher than the SI SNRs for all spatial frequencies in Fig. 3, for larger object support sizes, the MFBD SNRs for pixel-based PSF parameterization drop below the SI SNRs for normalized spatial frequencies around 0.25.

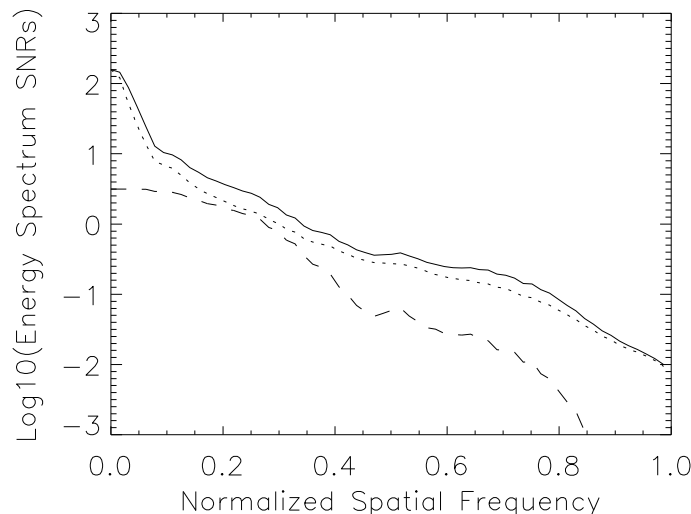


Fig. 3. Log_{10} plots of SI and MFBD SNRs as a function of normalized spatial frequency magnitude: MFBD SNRs for Zernike-based PSF parameterization (solid line), MFBD SNRs for pixel-based PSF parameterization (dotted line), and SI SNRs (dashed line). Parameter values are $D/r_o = 8$, $K = 10^4$, OCNR object, blur2 object support constraint, and the 99.9% PSF circular support constraint for the pixel-based PSF parameterization.

4.2 SNR dependence on D/r_o

The exploration of the dependence of the MFBD SNRs on D/r_o was guided by two observations. The first is the result from Subsection 4.1 that the MFBD SNRs as a function of spatial frequency are approximately proportional to the square root of $|O_n(f)|^2 E[H(f)]^2$ for all light levels. The second is that the SI SNRs are proportional to D/r_o only through $E[H(f)]^2$ in the low light level limit and are independent of D/r_o in the high light level limit. Based on these two observations, it was expected that the MFBD SNRs would depend on D/r_o only through the square root of $E[H(f)]^2$ for all light levels. This intuition was explored for all photon levels, for both objects, and for all three values of D/r_o : 8, 16, and 32. For each D/r_o value, MFBD SNRs were calculated for both pixel-based and Zernike-based PSF parameterizations. Each MFBD SNR result was then normalized by dividing it by the square root of the $|O_n(f)|^2 E[H(f)]^2$ term used in its calculation. If the MFBD SNRs depend only on D/r_o through the square root of $E[H(f)]^2$, the resulting plots should be the same for all D/r_o values; however, it was discovered that these normalized MFBD SNRs still depended on D/r_o . The plots in Figs. 4 and 5 illustrate this dependency. For these plots, $K=10^4$, and the OCNR object and the blur2 object support constraint were used. The plots in Fig. 4 are for MFBD SNRs with Zernike-parameterized PSFs, and the plots in Fig. 5 are for pixel-parameterized PSFs using the 99.9% PSF circular support constraint. Both the pixel-parameterized and Zernike-parameterized plots are approximately constant through the mid-spatial-frequency region (over which the square root of $E[H(f)]^2$ varies considerably), as they should be since the SNRs have already been shown to be qualitatively proportional to the square root of the $|O_n(f)|^2 E[H(f)]^2$. The interesting point to be made

from Figs. 4 and 5 is that the quantitative proportionality constant depends upon D/r_o ; in fact, the proportionality constant is an increasing function of D/r_o . This indicates a decrease in the sensitivity of the MFBD SNRs to atmospheric turbulence as compared to SI SNRs, in addition to the already-shown dependence on the square root of $E[H(f)]^2$. The proportionality constant has a stronger dependence on D/r_o for Zernike-based PSF parameterization than for pixel-based PSF parameterization. At this time, an expression for the mid-spatial-frequency dependence of the MFBD SNRs on D/r_o for either parameterization has not been derived. More research is planned to further understand this dependence.

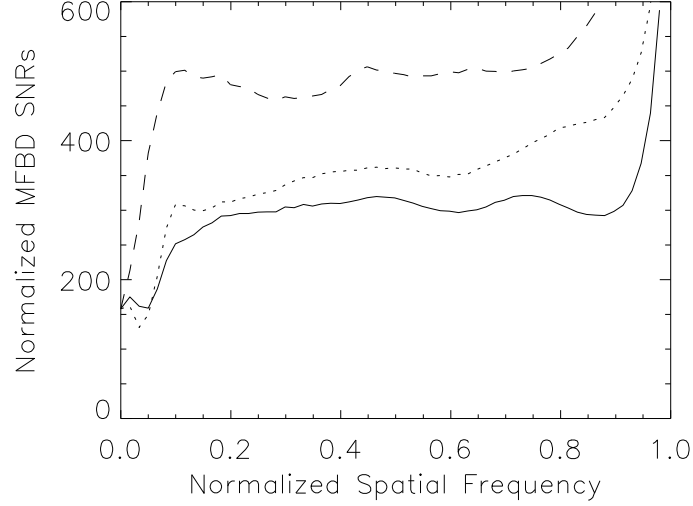


Fig. 4. Plots of Zernike-parameterized-PSF MFBD SNRs, each normalized by dividing it by the square root of the $|O_n(f)|^2 E[H(f)]^2$ term used in its calculation, as a function of normalized spatial frequency magnitude: $D/r_o = 8$ (solid line), $D/r_o = 16$ (dotted line), $D/r_o = 32$ (dashed line). Parameter values are $K = 10^4$, OCNR object, and blur2 object support constraint.

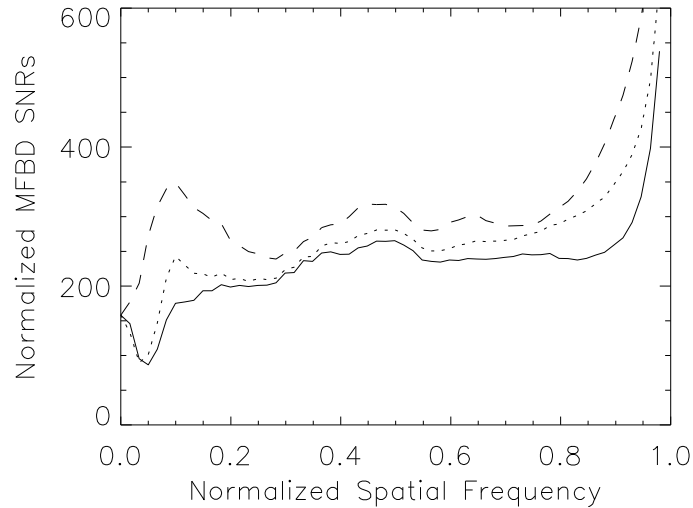


Fig. 5. Plots of pixel-parameterized-PSF MFBD SNRs, each normalized by dividing it by the square root of the $|O_n(f)|^2 E[H(f)]^2$ term used in its calculation, as a function of normalized spatial frequency magnitude: $D/r_o = 8$ (solid line), $D/r_o = 16$ (dotted line), $D/r_o = 32$ (dashed line). Parameter values are $K = 10^4$, OCNR object, blur2 object support constraint, and the 99.9% PSF circular support constraint.

4.3 SNR dependence on K

The dependence of the SI SNRs and the MFBD SNRs on K was explored for a variety of parameter combinations. From Eq.(4), it can be seen that the SI SNRs are proportional to K at low light levels and are independent of K at high light levels. The MFBD SNRs were discovered to be proportional to the square root of K for all light levels. Plots of SI SNRs, MFBD SNRs for Zernike-based PSF parameterization, and MFBD SNRs for pixel-based PSF parameterization are displayed in Figs. 6 and 7 for $K=10^2$ and $K=10^8$, respectively. For these results, $D/r_o=8$, the OCNR object, and the blur2 object support constraint were used. For the pixel-based PSF parameterization results, the 99.9% PSF circular support constraint was used. The low-light-level results displayed in Fig. 6 show that the SI and MFBD SNRs are comparable near zero spatial frequency, but then the $|O_n(f)|^2 E[H(f)]^2$ dependence of the SI SNRs causes them to decrease much more rapidly than the MFBD SNRs as spatial frequency magnitude increases. The high-light-level results displayed in Fig. 7 show the opposite trend; that is, the SI and MFBD SNRs differ most at the low spatial frequencies due to the upper limit of $M^{1/2}$ to the SI SNRs, but the differences decrease as spatial frequency magnitude increases due to the dependence of MFBD SNRs on the square root of $|O_n(f)|^2 E[H(f)]^2$. It can be seen for both cases, though, that the MFBD SNRs are always higher.

4.4 SNR dependence on object support constraint area

There is no dependence of the SI SNRs on object support constraint area, as can be seen in Eq.(4), because the standard way to reconstruct an image using SI techniques has no provision for including an object support constraint. On the other hand, including an object support constraint in MFBD algorithms is a common practice. For this reason, the impact of the size of the object support constraint area on the MFBD SNRs was explored and is now discussed.

It was discovered that the MFBD SNRs remain qualitatively proportional to the square root of $|O_n(f)|^2 E[H(f)]^2$ regardless of the size of the object support constraint area; however, the SNR at each spatial frequency is a decreasing function of the object support constraint area. To illustrate this latter point, the dependence of the MFBD SNRs on object support constraint area is shown in Fig. 8 for Zernike-based and pixel-based PSF parameterizations. The quantities plotted are the sums of the MFBD SNRs inside the telescope bandpass normalized by dividing each sum by the sum of the MFBD SNRs for the smallest object support constraint area. For these plots, $K=10^4$, $D/r_o=8$, and the OCNR object was used. For pixel-based PSF parameterization, the 99.9% PSF circular support constraint was used. The object support constraints used for the results were generated by blurring the true object support by square kernels that were 2, 4, 6, 8, 10, 14, and 18 pixels on a side. It can be seen from the two plots in Fig. 8 that the MFBD SNRs are a decreasing function of object support constraint area. It is interesting to note that the rate of decrease in the SNRs becomes less as the object support constraint area becomes larger. This implies that the biggest benefit from increasing the accuracy of an object support constraint comes when the accuracy is already quite good.

4.5 SNR dependence on PSF support constraint area for pixel-based PSF parameterization

There is no provision in standard SI algorithms to include a PSF support constraint because PSF information is included only in the modulus squared of the atmosphere/telescope transfer function. For MFBD algorithms that use pixel-based PSF parameterization, it is common to include a PSF support constraint. For this reason, the dependence of MFBD SNRs for pixel-based PSF parameterization on the PSF support constraint area was explored and is now discussed.

The quantities plotted in Fig. 9 are the sums of the MFBD SNRs inside the telescope bandpass normalized by dividing each sum by the sum of the MFBD SNRs for the smallest PSF support constraint area. For these plots, $K=10^4$, $D/r_o=8$, the OCNR object, and the blur2 object support constraint were used. The PSF support constraints were circles of increasing radius. The minimum radius resulted in 99% of the PSF energy being enclosed, while the maximum radius resulted in 99.99% of the PSF energy being enclosed. It can be seen from the plot in Fig. 9 that the same behavior of the MFBD SNRs is seen for increasing PSF support constraint area as was seen for increasing object support constraint area.

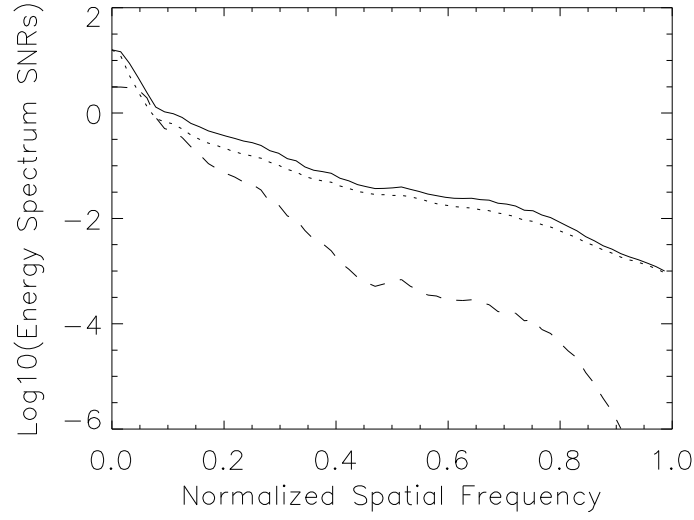


Fig. 6. Log_{10} plots of low-light-level energy spectrum SNRs as a function of normalized spatial frequency magnitude: MFBD SNRs for Zernike-based PSF parameterization (solid line), MFBD SNRs for pixel-based PSF parameterization (dotted line), and SI SNRs (dashed line). Parameter values are $D/r_o = 8$, $K = 10^2$, OCNR object, blur2 object support constraint, and the 99.9% PSF circular support constraint for the pixel-based PSF parameterization.

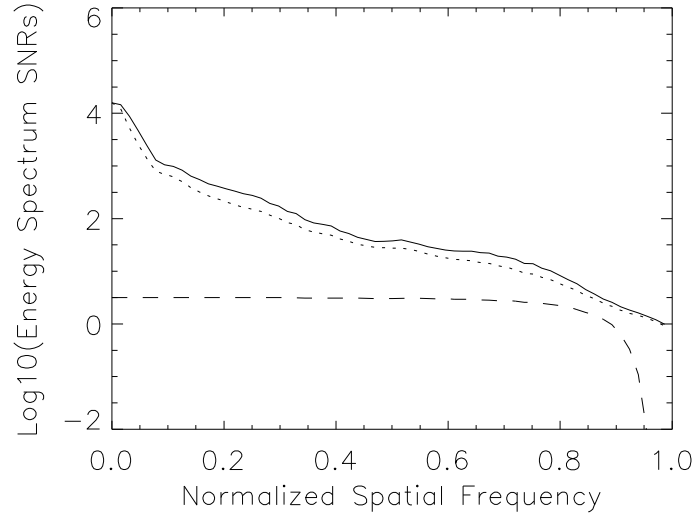


Fig. 7. Log_{10} plots of high-light-level energy spectrum SNRs as a function of normalized spatial frequency magnitude: MFBD SNRs for Zernike-based PSF parameterization (solid line), MFBD SNRs for pixel-based PSF parameterization (dotted line), and SI SNRs (dashed line). Parameter values are $D/r_o = 8$, $K = 10^8$, OCNR object, blur2 object support constraint, and the 99.9% PSF circular support constraint for the pixel-based PSF parameterization.

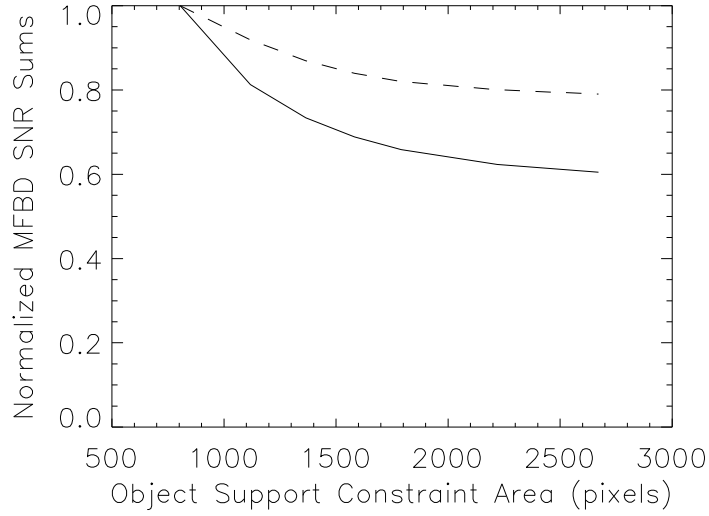


Fig. 8. Sums of MFB SNRs inside the telescope bandpass, normalized by dividing each sum by the MFB SNR sum for the smallest object support constraint area, as a function of object support constraint area: pixel-based PSF parameterization (solid line), and Zernike-based PSF parameterization (dashed line). Parameter values are $D/r_o = 8$, $K = 10^4$, OCNR object, and the 99.9% PSF circular support constraint for the pixel-based PSF parameterization.

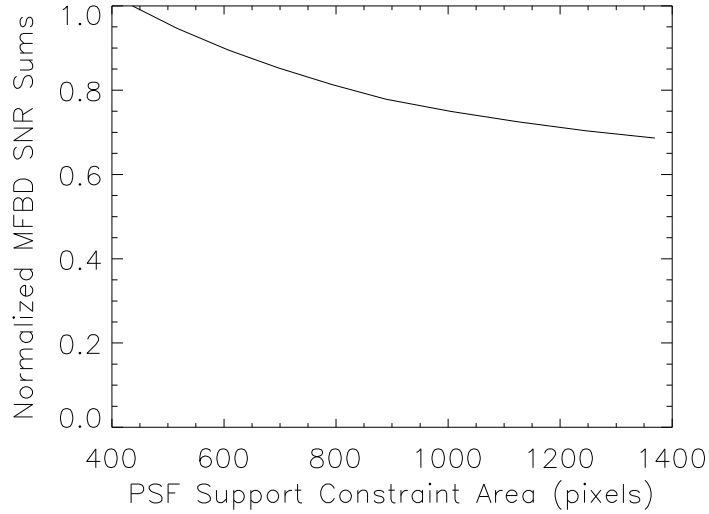


Fig. 9. Sums of MFB SNRs inside the telescope bandpass, normalized by dividing each sum by the MFB SNR sum for the smallest PSF support constraint area, as a function of PSF support constraint area. Parameter values are $D/r_o = 8$, $K = 10^4$, OCNR object, and blur2 object support constraint.

4.6 SNR dependence on read noise variance and M

To investigate the SNR dependence on read noise variance, consider the case where read noise dominates photon noise. For the SI SNRs, this occurs when the variance term $N^4 \sigma^4$ is much larger than the other terms in the denominator of

Eq.(4). It can be seen in this case that the SI SNRs are proportional to $N^{-2}\sigma^{-2}$, K^2 , and $|O_n(f)|^2 E[H(f)]^2$. Recall that there are two limiting cases when read noise is negligible: the high-light-level case ($K^4|O_n(f)|^4 E[H(f)]^2$ much greater than the other denominator terms), and the low-light-level case (K^2 much greater than the other denominator terms). The low-light-level SI SNRs are proportional to K and $|O_n(f)|^2 E[H(f)]^2$, while the high-light-level SI SNRs are independent of these values. Thus the impact of read noise dominating photon noise on the SI SNRs as compared to the converse case is to cause them to be proportional to $N^{-2}\sigma^{-2}$ and $|O_n(f)|^2 E[H(f)]^2$ regardless of the photon level, and increase the photon dependence from either none or K to K^2 .

For the MFBD SNRs, the impact of read noise dominating photon noise as compared to converse case follows a pattern similar to the low-light-level SI SNRs. The photon dependence increases from $K^{1/2}$ to K , and the read noise dependence goes from none to $N^{-1}\sigma^{-1}$. There is no change in the dependence of the MFBD SNRs on the square root of $|O_n(f)|^2 E[H(f)]^2$, D/r_o , object support constraint area, and PSF support constraint area.

Next, the dependence of the SNRs on M is discussed. It is easy to see from Eq.(4) that the SI SNRs are proportional to $M^{1/2}$ regardless of the photon level. For $M \gg 10$, the MFBD SNRs are also proportional to $M^{1/2}$. For smaller values of M , the MFBD SNRs depend on the structure of the individual atmospheric PSFs.⁶ This PSF-structure dependence occurs because of the few number of frames used in the estimation process. A similar dependence would be seen in SI SNRs if only a few frames are used; however, the SI SNR expression assumes that the individual structure of the PSFs has been averaged out so that the underlying statistical properties of the PSFs determine the SNRs.

5. CONCLUSIONS

A comparison of MFBD and SI SNRs associated with estimating an object's energy spectrum from a sequence of short-exposure atmospherically-blurred images of the object was given in this paper. The SI SNRs were calculated using the standard closed-form image energy spectrum expression, which implies that a perfect estimate of the speckle transfer function is available; thus, the SI SNRs are upper bounds to the achievable SI SNRs for real data. The MFBD SNRs were calculated using CRBs in place of variances due to the lack of an analytical expression for the variances; thus, the MFBD SNRs are upper bounds to the achievable MFBD SNRs.

It was shown that the MFBD SNRs are almost always greater than the associated SI SNRs at all spatial frequencies, and that they are both proportional to $M^{1/2}$ when $M \gg 10$. Other conclusions depend on the relative magnitudes of the photon noise and read noise variances. When photon noise dominates read noise, it was shown that the low-light-level SI SNRs are proportional to K and $|O_n(f)|^2 E[H(f)]^2$, while the MFBD SNRs are proportional to the square root of these quantities. The high-light-level SI SNRs are independent of K and $|O_n(f)|^2 E[H(f)]^2$, while the high-light-level MFBD SNRs are still proportional to the square root of K and $|O_n(f)|^2 E[H(f)]^2$. When read noise dominates photon noise, the SI SNRs are proportional to K^2 , $|O_n(f)|^4 E[H(f)]^2$, and $N^{-2}\sigma^{-2}$ for all light levels, while the MFBD SNRs are proportional to the square root of these quantities.

Unlike SI SNRs, MFBD SNRs depend on D/r_o through more than the $E[H(f)]^2$ term. Although the spatial frequency dependence of the MFBD SNRs is qualitatively equal to $E[H(f)]^2$ as D/r_o increases, the decrease in the MFBD SNRs is less than the decrease in $E[H(f)]^2$. In addition, MFBD SNRs are decreasing functions of the size of the object and PSF support constraint areas, while the SI SNRs are independent of these sizes since the SI SNR expression does not include the effects of using support constraints.

ACKNOWLEDGMENTS

The author thanks the Air Force Office of Scientific Research and the Air Force Research Laboratory for their financial support that made this research possible.

REFERENCES

- [1] Roggemann, M. C. and Welsh, B., [Imaging Through Turbulence], CRC Press, Boca Raton (1996).
- [2] Kundur, D. and Hatzinakos, D., "Blind image deconvolution," IEEE Signal Process. Mag. 13(3), 43-64 (1996).

- [3] D. Kundur and D. Hatzinakos, "Blind image deconvolution revisited," IEEE Signal Process. Mag. 13(6), 61-63 (1996).
- [4] Porat, B., [Digital Processing of Random Signals -Theory and Methods], Prentice-Hall, Englewood Cliffs (1994).
- [5] Gonzalez, R. C. and Woods, R. E., [Digital Image Processing], Addison-Wesley, Reading (1992).
- [6] Matson, C. L. and Haji, A., "Noise reduction in support-constrained multi-frame blind-deconvolution restorations as a function of the number of data frames and the support constraint sizes," Signal Recovery and Synthesis, 2007 OSA Technical Digest Series, paper SMB2 (2007).